

Analytic System Matrix Resolution Modeling in PET: An Application to Rb-82 Cardiac Imaging

A. Rahmim¹, M. A. Lodge¹, J. Tang¹, S. Lashkari², M. R. Ay²

¹Department of Radiology, Johns Hopkins University, Baltimore MD USA 21205

²Department of Medical Physics and Biomedical Engineering, Medical Sciences University of Tehran, Iran

Abstract—An area of growing interest in PET imaging has been that of incorporating increasingly more accurate system matrix elements into the reconstruction task, thus arriving at images of higher quality. This work explores application of an analytic approach which individually models and combines the various resolution degrading phenomenon in PET (inter-crystal scattering, inter-crystal penetration, photon non-collinearity and positron range), and does not require extensive experimental measurements and/or simulations. The approach is able to produce considerable enhancements in image quality. The reconstructed resolution is seen to improve from 5.1mm-7.7mm across the field-of-view (FoV) to ≈ 3.5 mm nearly uniformly across the FoV. Furthermore, phantom studies indicate clearly improved images, while similar significant improvements are seen for the particular task of Rb-82 cardiac imaging.

Keywords: Positron emission tomography, Image reconstruction, Image enhancement, Positrons, Compton scattering.

I. OVERVIEW AND MOTIVATION

In PET imaging, four processes are responsible for degrading image resolution: positron range, photon non-collinearity, inter-crystal scattering as well as penetration. Aside from improvements to PET detection (hardware), different reconstruction approaches have been proposed in the literature to model the aforementioned factors, with the aim of improving image resolution.

First, let us consider an image with J basis functions (usually voxels) and a histogrammed dataset with I projection bins. We then denote the system matrix as $\mathbf{P}=(p_{ij})_{I \times J}$, where each element p_{ij} models the probability that an event generated in voxel j is detected along line-of-response (LOR) i . Next, one may decompose [1] the system matrix into three components

$$\mathbf{P} = \mathbf{WGB} \quad (1)$$

Here, the matrix $\mathbf{B}=(b_{ij})_{J \times J}$ is used to account for image-based blurring effects, while the matrix $\mathbf{G}=(g_{ij})_{I \times J}$ contains the geometric probability terms relating each voxel j to an LOR i . In addition, the matrix $\mathbf{W}=(w_{ij})_{I \times I}$ can be used to account for sensitivity variations (i.e. due to attenuation and normalization) as well inter-crystal blurring effects.

An approach [2], [3] has been to model overall resolution blurring entirely into the image-space component \mathbf{B} of the system matrix. This approach is very straight-forward to implement, and produces images of higher quality. However, the

This work was supported by the National Institute of Health. Authors wish to thank T. Brown for providing clinical datasets used to create realistic simulations, F. Bengel and S. Sarkar for fruitful discussions, and Andrew Crabb for computational support.

method is somewhat *ad hoc* and in particular does not model the varying degrees of inter-crystal blurring in the projection space. The method is thus not suited to model the parallax effect. An approach developed in [4] proposed the use of space-variant blurring kernels to model this effect with some observed improvements, nevertheless the fundamental issue remains to be the fact that this approach does not allow modeling angular-dependent crystal blurring effects.

A more accurate approach [10] has been to collectively model inter-crystal scattering, penetration as well as photon non-collinearity in the projection space component \mathbf{W} of the system matrix. Monte Carlo simulations were then needed to be performed along a projection angle to extract the overall blurring kernels. The result were then assumed to apply to all other 2D projection angles.

An alternative approach [5]–[7] was instead to *analytically* calculate the angular-dependent inter-crystal penetration effects for the detector pairs. This resolution modeling method had the advantage that due to its analytical nature, was not *ad hoc* in nature and additionally made use of no simulations or experimental measurements. However, it neglected contributions due to crystal scattering, and only incorporated crystal penetration.

A new approach has been to make very accurate non-collimated [8] and collimated [9] point source measurements in the field-of-view (FoV) to extract the overall system matrix in a very elaborate manner. While the method results in impressive improvements in image quality, it requires extensive and very accurate point source measurements (e.g. using a positioning robot as done by the authors).

A new approach is investigated in this work, which takes the approach of analytically modeling each of the resolution degrading phenomenon, followed by their combination in the overall system matrix, thus not requiring extensive simulations or experimental measurements, and producing significantly improved image qualities. We describe each of these next.

II. DESCRIPTION OF METHOD

A. Positron Range

In the seminal work of Palmer and Brownell [11], a model of positron range was developed, and shown to closely agree with experimental [12] as well as simulated [13] results. It must be noted that since experimental measurements of positron range are performed in the projection space, the results are often depicted in that space. At the same time, to accurately model the effect of positron range in the reconstruction task, we must

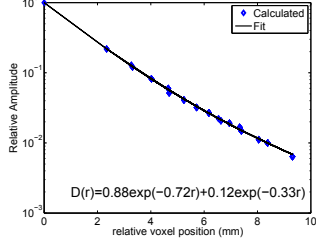


Fig. 1. The Rb-82 positron range, upon binning into appropriate voxels, is well-fit by a bi-exponential curve, as shown in this figure.

use the image-space component (\mathbf{B} in Eq. 1) of the system matrix, since its elements model inter-voxel contributions. As such, the fully 3D model of positron range was used in this work. This can be summarized as follows (which has been similarly incorporated in the simulation package SimSET [14]): for an isotope with an atomic number Z and endpoint energy E_{max} , the positron emission energy distribution $N(E)$ is given by:

$$N(E) = (E^{max} - E)^2 W p F(Z, W) \quad (2)$$

where E is the emission energy in MeV, $W=1+E/0.511$, $p=\sqrt{W^2-1}$, and

$$F(Z, W) = \frac{2\pi\eta}{1 - e^{-2\pi\eta}}; \eta = \frac{-ZW}{137p} \quad (3)$$

In the particular case of Rb-82, two end point energies exist ($E_1^{max}=3.379$ MeV and $E_2^{max}=2.603$ MeV with branching ratios of 0.833 and 0.117; note that Eq. 2 must be first normalized prior to weighted summation for these two energies).

For a given emitted positron energy E , the annihilation density is then modeled [11] as a 3D symmetric Gaussian:

$$D(\mathbf{r}, E) = \frac{1}{(\sqrt{2\pi}\sigma(E))^3} e^{-|\mathbf{r}|^2/2\sigma(E)^2} \quad (4)$$

$$\sigma(E) = \frac{R_{ex}(E)}{2d} \quad (5)$$

where d is the density (in g/cc) of the material the positron is traveling through, and R_{ex} is the extrapolated positron range, which for a material with an effective atomic weight A_{eff} and atomic number Z_{eff} is given by

$$R_{ex}(E) = \frac{b_1 E^2}{b_2 + E} \quad (6)$$

$$b_1 = \frac{4.569 A_{eff}}{Z_{eff}^{1.209}}; b_2 = \frac{1}{2.873 - 0.02309 Z_{eff}} \quad (7)$$

Values of A_{eff} and Z_{eff} for biological materials are relatively similar (for water: $A_{eff}=13.00$; $Z_{eff}=7.217$). We may finally compute the overall 3D distribution $\overline{D}(\mathbf{r})$:

$$\overline{D}(\mathbf{r}) = \int D(\mathbf{r}, E) N(E) dE \quad (8)$$

In our application of interest (Rb-82), the resulting distribution was then binned into voxels and then fit by a bi-exponential curve, as depicted in Fig. 1, which is subsequently used in definition of the system matrix.

B. Photon Non-collinearity

Due to small residual momentum of an emitted positron when it reaches the end of its range, the annihilated photons will exhibit non-collinearity. The angular distribution is approximately gaussian with FWHM of $\approx 0.5^\circ$. Technically, this effect has to be modeled in the geometric component G of the system matrix; however, as an approximation to considerably simplify the system matrix computation, one can assume photon non-collinearity is depth-independent and model it in the projection-space component W of the system matrix. The effect of blurring on spatial resolution using simple geometric calculations can be shown to be given by a gaussian with

$$FWHM = 0.5 \frac{\pi}{180} \times \frac{L}{4} = 0.0022 \times L \quad (9)$$

where L is the separation of the detector in coincidence, thus arriving at the non-collinearity blurring kernel $D_{non-col.}(x, z)$ along the radial x and axial z directions. Since this effect is independent from the crystal blurring effects, once those are extracted, they are convolved with $D_{non-col.}(x, z)$. This will be discussed next.

C. Inter-crystal scatter and penetration

In the present work, we have assumed (as studied below) that the inter-crystal scatter and penetration effects can be separately modeled and then convolved with one another. First, the penetration effect can be modeled using a knowledge of the 511-keV attenuation coefficient μ of the crystals, as well as the angle of incidence θ . As such, the 1D deposition distribution $p(x, \theta)$ tangential to the detector surface is given by:

$$p(x, \theta) = e^{-\mu x / \sin(\theta)} \quad (10)$$

Then, from the individual detectors' penetration model $p(x, \theta)$, the resulting penetration distribution $D_{penet.}(x, \theta)$ for the *coincidence* pair can be calculated, as similarly done in [5], [6], and is given by:

$$D_{penet.}(x, \theta) = \int_{x'} p(x', \theta) p(2x - x', \theta) dx' \quad (11)$$

Next, an assumption has been that it is the penetration effect (and not the scatter) that is highly angular-dependent, and for the latter we used measured projection data of a point source at the centre of the FoV (thus no parallax contribution), and determined the average radial and axial scatter blurring introduced by the scanner in the sinogram-space (we corrected for the non-collinearity effect via subtraction in squares), to arrive at an estimate of $D_{scatter}(r, z)$. Finally, in the present work, we arrive at the overall projection-space blurring kernel $D_{proj.}(x, z)$ via performing:

$$D_{proj.}(x, z, \theta) = D_{non-col.}(x, z) * D_{penet.}(x, \theta) * D_{scatter}(x, z) \quad (12)$$

where $*$ indicates a convolution.

Simulations: To study the separate modeling of inter-crystal scattering and penetration effects, we utilized the MCNP4C Monte Carlo code for detailed transport of 511keV photons originated from a point source at various angles of incidence θ from 0 to 45° (total of 50000 photons). We then performed

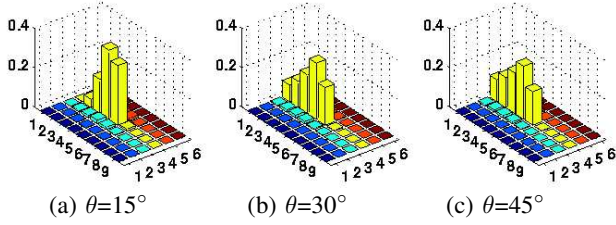


Fig. 2. Simulated crystal absorption profiles, shown here for photons incident at the crystal 5,4 (of a simulated 9x6-crystal block) at θ values of (a) 15° , (b) 30° and (c) 45° .

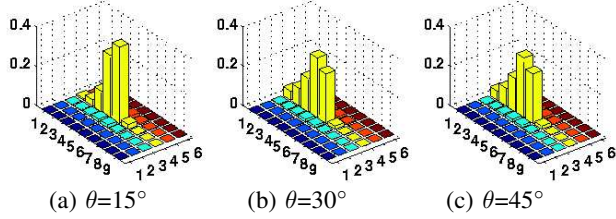


Fig. 3. Crystal absorption profiles calculated as described in text with standard $\mu=0.0755\text{mm}^{-1}$.

convolution operations between the penetration distributions at various angles (calculated using $\mu=0.0755$ (LYSO) in Eq. 10) and the scattering distribution (obtained at normal incidence) to arrive at overall estimate inter-crystal blurring kernels. Compared to the actual simulated blurring kernels, some mismatches can be observed as depicted in Figs. 2 and 3; in particular, the extent of contamination to nearby crystals appears underestimated. This is because we have observed (not shown) through these simulations that the scattered distribution is *not* symmetric and that it exhibits more scatter contributions in the direction of incidence.

There are a number of approaches to better model this effect: one may consider the use of asymmetric, angular-dependent scattering kernels as a solution. Another solution is to use a smaller μ value for the calculation of the parallax effect in order to effectively model the additional scatter contribution in the direction of incidence. Using a smaller $\mu=0.045$ as shown in Fig. 4, overall distributions closely matching the simulated distribution (Fig. 2) were observed. In the present work, we have continued to use the standard $\mu=0.0755$, while in the future, alternative approaches will be explored.

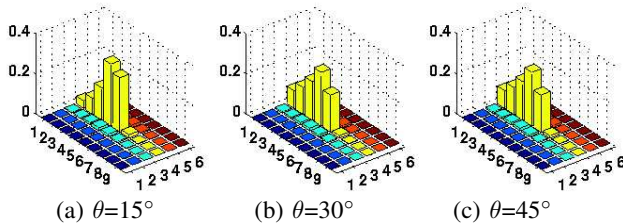


Fig. 4. Crystal absorption profiles calculated similar to Fig. 3 but instead using $\mu=0.045\text{mm}^{-1}$.

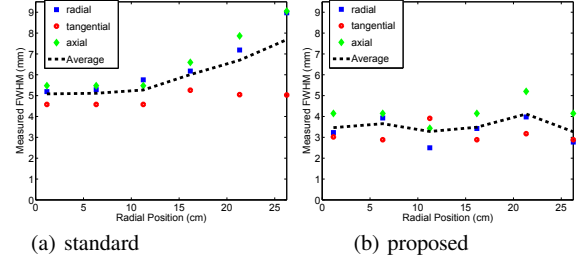


Fig. 5. (a) Improvements in resolution across the FoV is apparent upon inclusion of the proposed resolution modeling approach.

D. Resolution Modeled Reconstruction Algorithm

For compact representation [1], we use $\vec{s}=[s_1\dots s_J]^{tr}$, $\vec{n}=[n_1\dots n_J]^{tr}$, $\vec{\lambda}^m=[\lambda_1^m\dots\lambda_J^m]^{tr}$ to denote 1D vectors of image sensitivity, projection data and image intensity (estimated at iteration m), respectively (tr denotes the transpose). The standard EM algorithm is then written as:

$$\vec{\lambda}^{m+1} = \frac{\vec{\lambda}^m}{\vec{s}} \times \mathbf{P}^{tr} \left\{ \frac{\vec{n}}{\mathbf{P}\vec{\lambda}^m} \right\} \quad (13)$$

where vectorial multiplication and division operations are performed on an element-by-element basis. Upon substitution of Eq. (1) into the EM algorithm, this becomes:

$$\vec{\lambda}^{m+1} = \frac{\vec{\lambda}^m}{\vec{s}} \times \mathbf{B}^{tr} \mathbf{G}^{tr} \mathbf{W}^{tr} \left\{ \frac{\vec{n}}{\mathbf{WGB}\vec{\lambda}^m} \right\} \quad (14)$$

and the sensitivity image is given by $\vec{s} = \mathbf{B}^{tr} \mathbf{G}^{tr} \mathbf{W}^{tr} \vec{\Pi}$ where $\vec{\Pi}$ refers to a vector of all-ones.

III. METHODS, RESULTS AND DISCUSSION

Tomograph: Data were simulated for and acquired on the Discovery RX PET/CT scanner [15]. The scanner uses LYSO crystals of dimensions $4.2 \times 6.3 \times 30$ mm in the tangential, axial, and radial directions. The LYSO crystals are arranged into 9x6 blocks, and the scanner contains 24 rings and 630 crystals per ring.

Reconstruction: An OSEM reconstruction code was developed for the scanner, which in its non-resolution-modeling mode, highly resembled the performance of the standard clinical reconstruction software. Normalization and attenuation were incorporated in the system matrix, while estimated randoms and scattered events were incorporated in the denominator of the OSEM algorithm, with the images finally scaled by global decay and deadtime factors.

Point Sources: A Na-22 point source was placed at six positions radially across the FoV (from the center to $x=25\text{cm}$, each separated by 5cm), imaged for 3 minutes in each position, and reconstructed using different methods. The measured FWHM widths are shown in Fig. 5. It is clearly seen that the proposed resolution modeling significantly improves the resolution, and also results in better resolution uniformity across the FoV.

Contrast Phantom: To simultaneously study the effect of the proposed approach on both contrast and noise, a Jacczak phantom was scanned, with 4 hot spheres (diams. of 25, 16, 12 and 8 mm, hot:background=4:1, F-18 was used) and 3 cold

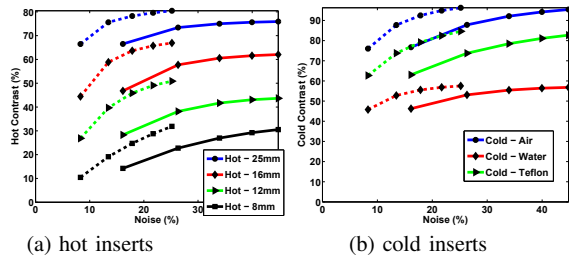


Fig. 6. Comparison of percent contrast vs. noise for the 4 hot and 3 cold inserts, for standard (solid) and proposed resolution-modeled (dotted) reconstructions (measurements are shown for the first five iterations).

sphere (25cm, filled with water, air, teflon). Plots of percent contrast vs. noise are shown in Fig. 6, and clearly demonstrated improved trade-off curves.

Simulation of Rb-82 Cardiac Imaging: The NCAT phantom was used in combination with the combined SimSET/GATE package to perform realistic simulations of Rb-82 cardiac imaging in the Discovery RX scanner, while the organ activity ratios with respect to the heart uptake were determined based on clinical cardiac PET studies (average of 12 patients at stress). We ran the simulation with the positron decay number nearly equivalent to a 12 sec acquisition (without gating) after the input function peaked.

The reconstructed percent contrast between the myocardium and stomach are plotted in Fig. 7 against the calculated noise (normalized standard deviation of voxels) in the myocardium. Without modeling Rb-82 positron range (i.e. only modeling non-collinearity, crystal scattering and penetration), we already see noticeable improvements in the contrast vs. noise trade-off, while the curves are further improved upon inclusion of the Rb-82 positron range model.

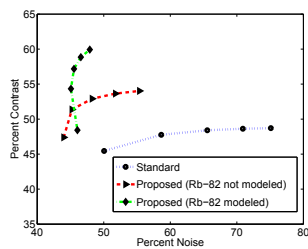


Fig. 7. Plots of contrast vs. noise for each of the 5 iterations of the various methods. The proposed methods, especially when also incorporating the Rb-82 model, show significant improvements in the trade-off curves.

For visual inspection, some reconstructed slices are also shown in Fig. 8 for the conventional approach (2 iterations) and the proposed method without and with positron range modeling (5 iterations each). It can be seen that the resolution modeled methods (especially the one with the Rb-82 model) result in less noisy images compared to two iterations of the standard method, while additionally better contrast can be detected (as also quantitatively demonstrated in Fig. 7).

In conclusion, the proposed analytic modeling approach was shown to result in images of significantly higher quality. Point- and extended-source phantom studies showed improved resolution, resolution uniformity, contrast and noise in the

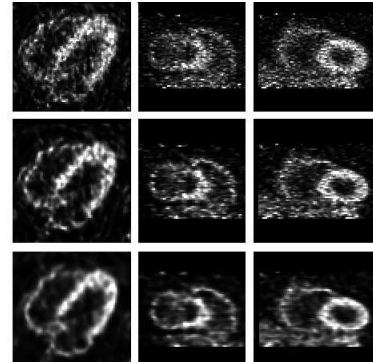


Fig. 8. Slices through images reconstructed using (top) the conventional approach (2 iterations), (top) the proposed method without positron range modeling (5 iterations), and (bottom) the proposed method while also modeling Rb-82 positron range (5 iterations). No post-smoothing has been used.

images. For the particular application of Rb-82 cardiac imaging, images of significantly higher quality and quantitative accuracy were obtained.

REFERENCES

- [1] A. J. Reader *et al.*, "One-Pass List-Mode EM Algorithm for High-Resolution 3-D PET Image Reconstruction Into Large Arrays", *IEEE Trans. Nucl. Sci.* vol. 49, pp. 693-699, 2002.
- [2] F. C. Sureau *et al.*, "Improved Clinical Parametric Imaging Using List-Mode Reconstruction via Resolution Modeling", *IEEE NSS/MIC Conf. Record*, vol. 6, pp. 3507-3510, 2006.
- [3] A. J. Reader *et al.*, "EM Algorithm System Modeling by Image-Space Techniques for PET reconstruction", *IEEE T. Nucl. Sci.*, vol. 50, pp. 1392-1397, 2003.
- [4] A. Rahmim *et al.*, "Space-variant and anisotropic resolution modeling in list-mode EM reconstruction", *IEEE Nucl. Sci. Symp. Conf. Record*, vol. 5, pp. 3074-3077, 2003.
- [5] R. Lecomte, G. Lamoureux, and D. Schmitt, "Geometry study of a high resolution pet detection system using small detectors", *IEEE Trans. Nucl. Sci.*, vol. 31, pp. 556-561, 1984.
- [6] D. Schmitt, B. Karuta, C. Carrier, and R. Lecomte, "Fast point spread function computation from aperture functions in high-resolution positron emission tomography", *IEEE Trans. Med. Imag.*, vol. 7, pp. 2-12, 1988.
- [7] V. V. Selivanov, Y. Picard, J. Cadorette, *et al.*, "Detector response models for statistical iterative image reconstruction in high resolution PET", *IEEE Trans. Nucl. Sci.*, vol. 47, pp. 1168-1175, 2000.
- [8] V. Y. Panin, F. Kehren, H. Rothfuss, D. Hu, C. Michel and M. E. Casey, "PET reconstruction with system matrix derived from point source measurements", *IEEE Trans. Nucl. Sci.*, vol. 53, pp. 152, 2006.
- [9] V. Y. Panin, F. Kehren, C. Michel, and M. Casey, "Fully 3-D PET reconstruction with system matrix derived from point source measurements", *IEEE Trans. Med. Imag.*, vol. 25, pp. 907-921, 2006.
- [10] J. Qi, R. M. Leahy, H. Chinghan, T. H. Farquhar, and S. R. Cherry, "Fully 3D Bayesian image reconstruction for the ECAT EXACT HR+", *IEEE Trans. Nucl. Sci.*, vol. 45, pp. 1096-1103, 1998.
- [11] M. R. Palmer and G. L. Brownell, "Annihilation density distribution calculations for medically important positron emitters", *IEEE Trans. Med. Imag.*, vol. 11, pp. 373-378, 1992.
- [12] S. E. Derenzo, "Mathematical removal of positron range blurring in high resolution tomography", *IEEE Trans. Nucl. Sci.*, vol. 33, pp. 546-549, 1986.
- [13] M. R. Palmer, X. Zhu, and J. A. Parker, "Modeling and simulation of positron range effects for high resolution PET imaging", *IEEE Trans. Nucl. Sci.*, vol. 52, pp. 1391-1395, 2005.
- [14] R. L. Harrison, M. S. Kaplan, S. D. Vannoy, and T. K. Lewellen, "Positron range and coincidence non-collinearity in SimSET", *IEEE NSS/MIC Conf. Record*, vol. 3, pp. 1265-1268, 1999.
- [15] B. J. Kemp, C. Kim, J. J. Williams *et al.*, "NEMA NU 2-2001 Performance Measurements of an LYSO-Based PET/CT System in 2D and 3D Acquisition Modes", *J. Nucl. Med.*, vol. 47, pp. 1960-1967, 2006.